actuators

MDPI

Article

Multiphysical Simulation, Model Order Reduction (ECSW) and Experimental Validation of an Active Magnetic Bearing

Johannes Maierhofer *, Christoph Dietz, Oliver M. Zobel and Daniel J. Rixen

Chair of Applied Mechanics, Department of Mechanical Engineering, TUM School of Engineering & Design, Technical University of Munich, 85748 Garching, Germany; christoph.dietz@tum.de (C.D.); oliver.zobel@tum.de (O.M.Z.); rixen@tum.de (D.J.R.)

* Correspondence: j.maierhofer@tum.de

Abstract: Model order reduction techniques can be used during the operation phase of a product to generate virtual sensor outputs and enable diagnosis and monitoring systems. This contribution shows an approach with the example of an active magnetic bearing. The reduced model is used to calculate a non-measurable physical quantity (here force) and uses a measurable quantity (temperature) to check for plausibility. As a test case, the dynamic force response under the influence of varying eddy currents due to temperature changes is investigated. Using a special test rig with a 6-dof force measurement platform, the effects are shown and the simulation results are validated.

Keywords: active magnetic bearing; multiphysical simulation; model order reduction; hyper-reduction; nonlinear magnetodynamics

Citation: Maierhofer, J.; Dietz, C.; Zobel, O.M.; Rixen, D.J. Multiphysical Simulation, Model Order Reduction (ECSW) and Experimental Validation of an Active Magnetic Bearing. *Actuators* **2022**, *11*, 169. https://doi.org/10.3390/act11060169

Academic Editors: Richard M. Stephan, Afonso Celso Del Nero Gomes and José Andrés Santisteban

Received: 27 May 2022
Accepted: 14 June 2022
Published: 17 June 2022

1. Introduction

Flywheel energy storage systems (FESSs) could potentially be one building block for the answer to the question of what could be a stable and sustainable energy supply in the future in the context of strongly fluctuating renewable energy sources. As shown in Figure 1, generic FESSs consist of a rotor supported by two magnetic bearings which carries an inertia mass and a motor-/generator-unit. The idea is simple: a spinning rotor stores energy in the form of kinetic energy [1]. By increasing the rotational speed, a surplus of electrical energy can be stored mechanically. At other times, the rotor can be slowed down and the energy is drawn out. The principle holds some major drawbacks: to achieve high efficiency, all types of friction need to be avoided as much as possible. Therefore, the rotor is supported by active magnetic bearings (AMBs). Active magnetic bearings are typical mechatronic machine elements to support rotor systems by levitating the shaft in a magnetic field. A second drawback arises from the high energy density in the system, which demands that safe operation has to be guaranteed at all times [2]. A monitoring system is therefore a necessary feature. One possible approach which makes use of a detailed simulation (also known as digital twin) is discussed in this paper. To enable standalone monitoring systems that are not dependent on the cloud or network infrastructure, the so-called *edge computing* approach should be favored. The application runs on rather low-end computing devices close to the source of the data [3,4].

This contribution focuses on the methodical investigation of the simulation, experimental calibration and generation of a reduced-order model of one active magnetic bearing. In this paper, an eight-pole, radial active magnetic bearing is investigated. This consists of four individually controllable electromagnets and operates in differential mode (more information in [2]). The bearing itself can be seen in Figure 9, where it is mounted on a calibration test rig. Additionally, a 2D-model of the bearing is presented in Figure 6.

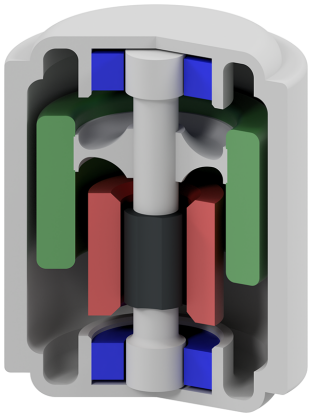

Figure 1. Schematic flywheel energy storage system (FESS) wherein red—stator; green—rotor with inertia; and blue—active magnetic bearing.

2. Monitoring Approach

The idea of the proposed monitoring approach is depicted in Figure 2 and is reminiscent of the concept of model predictive controllers. In a first step, the currents in the coils are recorded during steady state operation for a few seconds. Together with the initial conditions, the simulation is now performed, using the recorded currents as load input. The results predict the future state of the magnetic bearing. In the meantime, the real quantities including that of temperature also evolve in the bearing. Now, a comparison of the actual temperature with the predicted temperature is performed. If the difference is within a given tolerance, we can trust the simulation and readout virtual sensor values, such as forces. This force can then be fed to another monitoring system or simulation which finally gives the overall health status of the plant system. If the actual temperature is not near the simulated temperature, the simulation cannot be trusted. Various reasons could be at the origin of the deviation. A fault detection system will then apply different fault modes to the simulation until they match again.

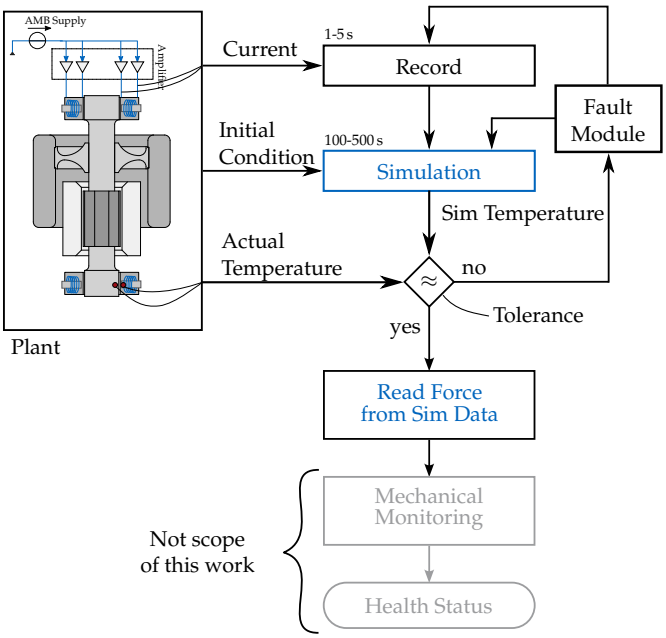

Figure 2. Monitoring scheme for the AMB. The simulation is fed with the measured currents and simulates the magnetic bearing. A comparison of the measured temperature with the simulated temperature gives a hint whether the simulation matches reality and can therefore be trusted.

We conclude that, in order to build a reliable monitoring system, a precise model of the system is needed that is also capable of running with as low computational effort as possible. This is the point at which the idea of model order reduction is highly suitable. A detailed description of the magnetodynamic simulation and hyper-reduction is found in [5].

3. Multiphysical Simulation

First, a full-order model must be set up to capture all relevant physical effects. In the following, the partial differential equations for the magnetodynamics and the thermodynamics are presented and a coupled finite element model is derived. Similar approaches are discussed in [6,7].

3.1. Governing Equations

Starting from *Maxwell's equations* for the electrodynamics, a few assumptions are made which simplify the equations for the application of electromagnetism in the low frequency range. More information on a detailed derivation is given in [5]. The first equation to consider is *Ampere's law* (1) where the current densities $\boldsymbol{j}$ in the coils lead to a magnetic field $\boldsymbol{H}$, see Equation (1), which is related to the magnetic flux density $\boldsymbol{B}$, with the nonlinear material parameter μ, as shown in Equation (3). According to *Faraday's law,* a change in the magnetic flux density ($\boldsymbol{B}$) results in an electrical field $\boldsymbol{E}$, as shown in Equation (2).

$$\nabla \times \boldsymbol{H} = \boldsymbol{j} \tag{1}$$

$$\nabla \times \boldsymbol{E} = -\frac{\partial \boldsymbol{B}}{\partial t} \tag{2}$$

$$B = \mu(B)H \tag{3}$$

For higher flux densities ($\|\boldsymbol{B}\| > 1\,\mathrm{T}$), the magnetic permeability μ of the ferromagnetic rotor and stator decreases significantly. To model this nonlinear material behavior, two generic, isotropic material laws are introduced and (later) tuned to fit the experimental setup:

$$\mu_{\mathrm{Rotor}}(B) = \left(\frac{400}{1 + 0.4(B/\mathrm{T})^8} + 1\right)\mu_0 \tag{4}$$

$$\mu_{\mathrm{Stator}}(B) = \left(\frac{2000}{0.4 + (B/\mathrm{T})^8} + 1\right)\mu_0 \tag{5}$$

The corresponding BH-curves are shown in Figure 3 together with the data (gray dashes) from the datasheets of the assumed material for the stator (thyssenkrupp, M270-35A according to DIN EN 10 106). For the rotor, a piece of material was measured at a partner.

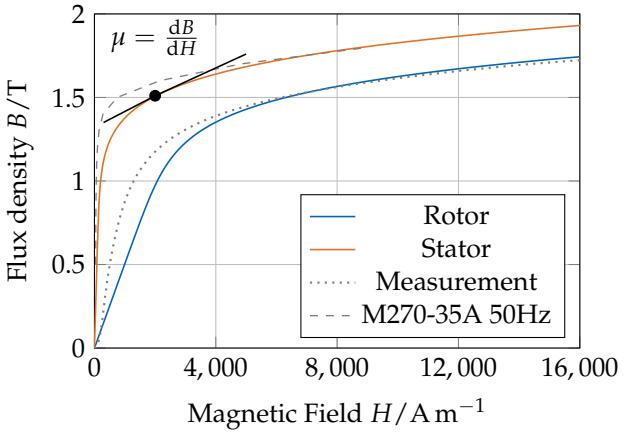

Figure 3. Generic material laws for the rotor and stator in comparison to data from the datasheets.

For varying currents, the magnetic field changes in time and induces the rotation of the electrical field $\boldsymbol{E}$, Equation (2). The induced electrical field causes so-called eddy currents which are described by *Ohm's law* where we consider that the conductivity σ is a function of temperature T (more information on the physics of conductivity in metals [8]):

$$\boldsymbol{j}_{\text{eddy}} = \sigma(T)\boldsymbol{E} \tag{6}$$

The eddy current itself has an effect on the magnetic field $\boldsymbol{B}$ via Equation (1). For higher frequencies, the electromagnetic field is concentrated in the boundary regions because the local eddy-currents prohibited the field to further propagate in the material. This is known as the skin-effect [9]. The dissipating eddy currents lead to a temperature rise in the bearing, which has a negative effect on the electrical conductivity σ as shown in Figure 4.

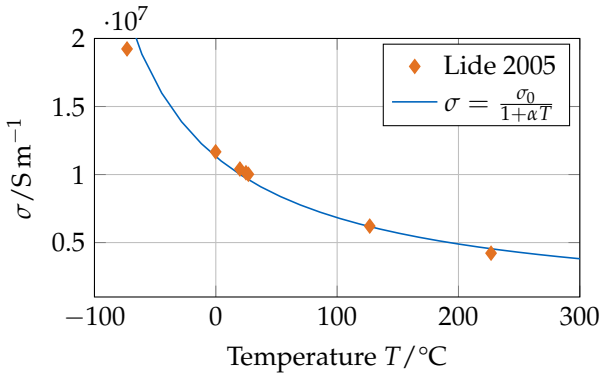

Figure 4. Nonlinear material law for the electrical conductivity of iron with $\sigma_0 = 10\,\text{MS/m}$ and $\alpha = 0.0058\,1/\text{K}$ in comparison to [10].

The specific power loss can be computed by:

$$q_{\text{heat}} = \frac{\|\boldsymbol{j}_{\text{eddy}}\|^2}{\sigma(T)} \tag{7}$$

To model the temperature evolution in the magnetic bearing, q_{heat} is used as the source term in the non-stationary heat equation:

$$\rho c \frac{\partial T}{\partial t} - \nabla \cdot \lambda \nabla T = q_{\text{heat}} \tag{8}$$

Here, ρ denotes the material density, c denotes the specific heat capacity, and λ denotes the thermal conductivity. All thermal properties are assumed to remain constant in the scope of this work.

3.2. Fem-Discretization

To solve the partial differential equations, a vector potential $\boldsymbol{A}$ is introduced with the definition Equation (9).

$$\boldsymbol{B} = \nabla \times \boldsymbol{A} \tag{9}$$

The electrical conductivity is assumed to be temperature-dependent but homogeneous across the stator and rotor. As [11] pointed out, in this case, both the magnetic and the electric field can be derived from the modified vector potential $\boldsymbol{A}$ as shown in Equation (10) where j_0 is the imposed current density.

$$\nabla \times \left(\frac{1}{\mu(\boldsymbol{A})} \nabla \times \boldsymbol{A} \right) = j_0 - \underbrace{\sigma(T) \frac{\partial \boldsymbol{A}}{\partial t}}_{\text{Eddy current}} \tag{10}$$

The discretization by finite elements results in a nonlinear model with primary variable $\boldsymbol{u}_E$ denoting the discretized vector potential solution. The model exhibits a nonlinear internal current vector (here called internal forces by analogy to mechanical problems), which stems from the material nonlinearity in Figure 3. The mass matrix (called as such in reference to mechanical problems and originating from the last term in Equation (10)) includes the electrical conductivity and hence depends on the discretized temperature solution $\boldsymbol{u}_T$. After discretization, the equations for the thermo-magneto-electric system are of the form:

$$\boldsymbol{M}_E(\boldsymbol{u}_T)\dot{\boldsymbol{u}}_E + \boldsymbol{g}(\boldsymbol{u}_E) = \boldsymbol{f}(\boldsymbol{j}_0) \tag{11}$$

For the thermal problem, a linear finite element model is used, where the r.h.s. depends on the eddy currents and the temperature solution $\boldsymbol{u}_T$ itself.

$$\boldsymbol{M}_T\dot{\boldsymbol{u}}_T + \boldsymbol{K}\boldsymbol{u}_T = \boldsymbol{f}(\boldsymbol{j}_{\text{eddy}}, \boldsymbol{u}_T) \tag{12}$$

Since the magnetodynamic model in Equation (11) and the thermal model in Equation (12) are fully coupled, a staggered solution scheme is proposed.

3.3. Time Integration

In this application, the temperature changes much more slowly than the electrodynamics (minutes/hours vs. milliseconds). Therefore, it is reasonable to perform a fully coupled simulation only for a small time frame, e.g., one magnetodynamic period. During this phase, the specific power loss in Equation (7) is averaged and then fed into the thermal model as a constant heat source. The temperature development can then be computed for a much longer time frame T. Subsequently, the electrodynamics have to be recalculated since the electrical conductivity has changed with the temperature. Using this alternating iteration strategy (Figure 5), the long-term force and temperature development can be computed with comparably low computational effort.

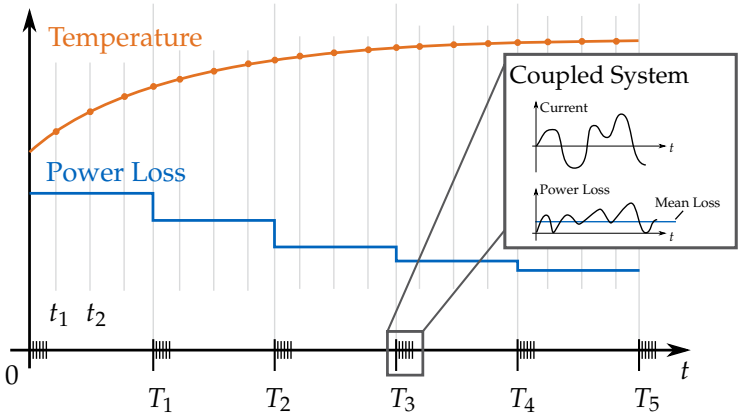

Figure 5. Timeintegration strategy with t_i being the magnetodynamic period and T_j denoting the large timestep used for the time integration of the thermodynamic model.

The time integration itself is performed using the backward Euler algorithm with k indicating the timestep. For the magnetodynamic domain Equation (11), the solution $\boldsymbol{u}_{E,k+1}$ for the next timestep t_{k+1} is then found with a Newton–Raphson scheme. For the thermal domain in Equation (12), only a linear solution is needed to find $\boldsymbol{u}_{T,k+1}$. Note the difference in the two timesteps $\Delta t = t_{k+1} - t_k$ and $\Delta T = T_{k+1} - T_k$, as seen in Figure 5.

$$\boldsymbol{M}_E(\boldsymbol{u}_{T,k})\boldsymbol{u}_{E,k+1} + \Delta t\boldsymbol{g}(\boldsymbol{u}_{E,k+1}) = \boldsymbol{M}_E(\boldsymbol{u}_{T,k})\boldsymbol{u}_{E,k} + \Delta t\boldsymbol{f}_{k+1}(\boldsymbol{j}_0) \tag{13}$$

$$(\boldsymbol{M}_T + \Delta T\boldsymbol{K})\boldsymbol{u}_{T,k+1} = \boldsymbol{M}_T\boldsymbol{u}_{T,k} + \Delta T\boldsymbol{f}_{k+1}(\boldsymbol{j}_{\text{eddy}}, \boldsymbol{u}_T) \tag{14}$$

3.4. Geometry and Mesh

Figure 6 shows the 2D finite element model of the magnetic bearing. This consists of the rotor and stator (conductive domain) and the coils. Both are surrounded by air, which is a further simplification compared to the real system depicted in Figure 9 in Section 5. To model the heat loss across the stator boundaries into the housing, a heat transfer coefficient α is introduced and calibrated on the test rig (cf. Section 5). The material behavior of the rotor and stator is modeled by the nonlinear magnetization curves presented in Figure 3 and the temperature-dependent electrical conductivity of iron depicted in Figure 4. The magnetization behavior of the coils is equivalent to air ($\mu_{\text{copper}} = \mu_0$).

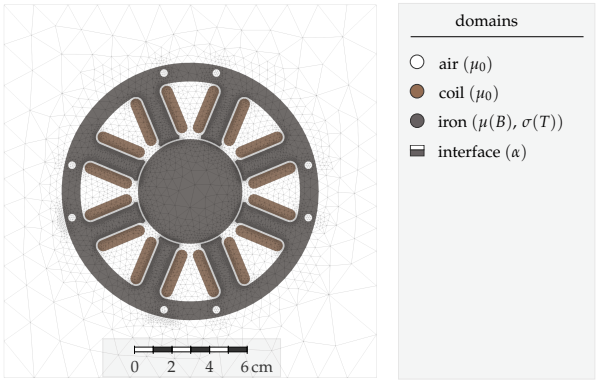

Figure 6. Two-dimensional model of an active magnetic bearing with finite element mesh.

In order to accurately model the full electrodynamics in the conductive domain, the mesh must fulfill certain requirements. Due to the skin effect, the element size (here defined as the maximal edge length) in the boundary region should be smaller than half of the skin-depth δ [12]:

$$h < \frac{1}{2}\delta \qquad \text{with} \quad \delta = \frac{1}{\sqrt{\pi f \mu \sigma}} \tag{15}$$

For a frequency f of 100 Hz, $\mu_r = 5000$ and $\sigma = 2 \times 10^6\,\mathrm{S\,m^{-1}}$ the element size on the iron boundary has to be smaller than 0.25 mm. Furthermore, it is suggested to increase the element size exponentially towards the inner of the iron parts. The fine spatial discretization leads to a very high dimensional model with a large number of dof. The mesh used for this work (Figure 6) provides an element size of approximately 0.25 mm to 25 mm from the iron–air boundary to the outside air volume. Thus, as a rough estimation, the simulation quality will not be appropriate for simulation frequencies above 100 Hz. On the other hand, a more refined mesh makes it impossible to solve fully on simple desktop machines.

3.5. Force Computation

The resulting total magnetic force on the rotor is computed by applying the principle of virtual work which is realized as a finite difference. Therefore, the rotor domain and its nodes are displaced by a small displacement Δx and the change in co-energy W' is observed by integration over the finite element domain Ω. The force is then obtained from:

$$F = \frac{\Delta W'}{\Delta x} \tag{16}$$

The co-energy is used to measure the amount of energy in the system that can be transformed into mechanical work. It can be computed by subtracting the magnetic energy W from the energy Π. The relation between energy W and co-energy W' is visualized in Figure 7. The sum of both is denoted as Π.

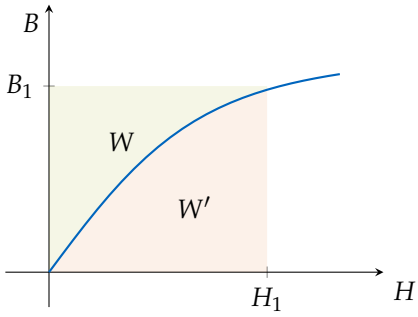

Figure 7. Magnetic energy and co-energy for a nonlinear material.

$$W' = \Pi - W \tag{17}$$

$$= \int_\Omega H_1 \cdot B_1 \, \mathrm{d}\Omega - \int_\Omega \int_0^{B_1} H(\tilde{B}) \, \mathrm{d}\tilde{B} \, \mathrm{d}\Omega \tag{18}$$

In Equation (18), H_1 and B_1 denote the terminal values which are obtained from the magnetodynamic solution via Equation (9).

4. Model Order Reduction

Model order reduction can generally either be used to accelerate the development process by generating faster simulations that can perform better in optimization algorithms or during the operation phase of a product, where slim models are needed to perform predictions on the health status of the machine. Such models enable the generation of virtual sensor outputs as well as diagnosis and monitoring systems. In this work, a reduced-order model should be derived for the latter.

Since the models for the magnetodynamics and the thermodynamics are uncoupled within the time integration strategy proposed in Section 3.3, both models can be reduced independently.

4.1. Thermal Model

For the linear thermal model (scalar temperature field vector $\boldsymbol{u}_T$), a simple projection to a subset of thermal modes is sufficient. The reduction basis is denoted by $\boldsymbol{V}_T$, whereas the generalized temperature coordinates are written as $\boldsymbol{q}_T$.

$$\boldsymbol{u}_T = \boldsymbol{V}_T \boldsymbol{q}_T \tag{19}$$

The thermic profile of the bearing can be mostly covered by the two thermal rigid body modes with temperature equally distributed between the rotor and the stator, respectively. As a positive side effect, a homogeneous temperature solution is enforced in the rotor and stator, which was also an assumption in the derivation of the governing electrodynamic equations (cf. Section 3.1). The Galerkin projection of Equation (12) onto $\boldsymbol{V}_T$ yields a 2×2 system for the thermodynamics:

$$\boldsymbol{M}_{r,T} \dot{\boldsymbol{q}}_T + \boldsymbol{K}_{r,T} \boldsymbol{q}_T = \boldsymbol{V}_T^T \boldsymbol{f}(j_{\mathrm{eddy}}, \boldsymbol{q}_T) \tag{20}$$

4.2. Magnetodynamic Model

In comparison, the magnetodynamic model exhibits nonlinearity and hence a data-based approach is used to construct a proper basis. It is computed by performing a proper orthogonal decomposition (POD) on a set of full solution vectors (see [5] for details). Tests showed that the magnetodynamics can be captured by only a few dominant pod-modes. Truncating the basis leads to the reduction basis $\boldsymbol{V}_E$.

$$\boldsymbol{u}_E = \boldsymbol{V}_E \boldsymbol{q}_E \tag{21}$$

The projection of the full magnetodynamic model (Equation (11)) onto the reduction basis $\boldsymbol{V}_E$ yields:

$$\boldsymbol{M}_{r,E}\dot{\boldsymbol{q}}_E + \boldsymbol{V}_E^T\boldsymbol{g}(\boldsymbol{V}_E\boldsymbol{q}_E) = \boldsymbol{V}_E^T\boldsymbol{f}(j_0) \tag{22}$$

Unexpectedly, the reduced model in Equation (20) does not lead to significant computational acceleration, since the full nonlinear current vector has to be assembled by evaluating the contribution of every single element of the FE mesh. Furthermore, the current vector is subsequently projected onto the reduction basis, which may even lead to higher computational costs than solving the full model [13].

4.3. ECSW-Method

Computational acceleration can be achieved by reducing the assembly process of the nonlinear current vector such that the nonlinearity only has to be evaluated on a subset $\tilde{\epsilon}$ of elements. These elements form the so-called reduced mesh. The idea is to preserve the virtual work of the reduced currents by introducing weighting factors ζ_e for each element of the reduced mesh [13]. The method is therefore called *energy-conserving sampling and weighting* (ECSW). A detailed insight into the application of ECSW on magnetodynamic systems can be found in [5]. Here, only a very short summary of the theory is given.

The elements and corresponding weights are found within a training process which requires a couple of solutions of the full model. The nonlinear internal current vector $\boldsymbol{g}$ is then approximated by only evaluating the nonlinearity of the elements of the reduced mesh Equation (23). Therefore, the element selection occurs with the localization matrix $\boldsymbol{L}_e$. The element results are then directly projected into the subspace spanned by $\boldsymbol{V}$. The same procedure is also applied to approximate the tangential stiffness matrix Equation (24), which is used within the Newton–Iteration scheme to solve the nonlinear equations.

$$\boldsymbol{g}_{r,\mathrm{ECSW}} = \sum_{e\in\tilde{\epsilon}} \zeta_e \boldsymbol{V}^T\boldsymbol{L}_e^T\boldsymbol{g}_e(\boldsymbol{L}_e\boldsymbol{V}\boldsymbol{q}) \tag{23}$$

$$\boldsymbol{K}_{r,\mathrm{ECSW}} = \sum_{e\in\tilde{\epsilon}} \zeta_e \boldsymbol{V}^T\boldsymbol{L}_e^T\boldsymbol{K}_e(\boldsymbol{L}_e\boldsymbol{V}\boldsymbol{q})\boldsymbol{L}_e\boldsymbol{V} \tag{24}$$

In Figure 8, the result of one exemplary ECSW training process is shown. The colored elements are the chosen elements with their weight encoded by color.

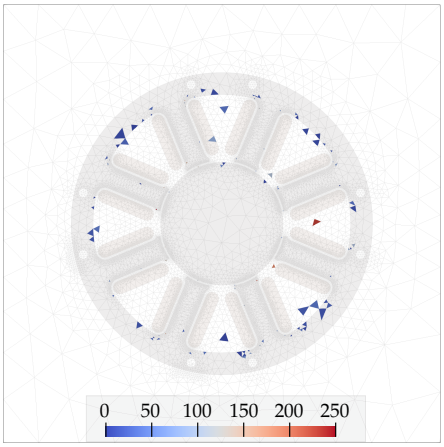

Figure 8. Exemplary ECSW elements and corresponding weights of the reduced mesh.

4.4. Setup of the Reduced Model

As the ECSW method in combination with the POD projection is a data-driven method, the first task is to find an appropriate training set. It would be beyond the scope of this paper to describe all the prestudies and considerations of generating the reduced model. To generate the snapshots for the PODs and for the internal forces used to train the ECSW (i.e., finding an appropriate reduced set of elements and the corresponding weights), a sinusoidal

time history (called also trajectory here) for the imposed currents (load) is imposed and time solutions are computed for the lower and upper extreme load amplitudes and frequencies (shown in Table 1) expected during monitoring. To train the ECSW, 10 snapshots per period are used. As the system is at rest in the beginning, the transient behavior is also captured by the snapshots.

Table 1. Four simulation setups to find the basis and to train the ECSW element selection at a constant temperature of $T = 20\,°C$.

j/A/mm^2	f/HZ	Δt/ms	n_{Steps}
1	10	10	10
1	100	1	10
4	10	10	10
4	100	1	10

The computations are performed on a mid-class desktop computer with general characteristics and installed environments as listed in Table 2.

Table 2. Computer configuration with installed environments.

Processor	Intel(R) Core(TM) i7-8850H @ 2.60 GHz
RAM	16 GB
OS	macOS 12.4
Python	3.8.10
NGSolve	6.2201

From that training set, reduced models with three different levels of accuracy for the approximation of the reduced internal currents (with ECSW) were tested. The three models result in an increase in elements in the subset $\tilde{\epsilon}$. The first result in terms of computational effort is shown at this point in Table 3. The first section shows the duration of the element selection process for the three different hyper-reduction levels (error in the energy approximation expressed by τ).

The second section of the table shows the computational time for key steps of the time integration simulation. The computational costs for one timestep is compared between the full model and the reduced-order models (ECSW). Since the computational times vary depending on the actual load step and system state, all times are averaged over the whole trajectory of the training simulation. The step *Residual* lists the costs required to evaluate the nonlinearity and to assemble the (reduced) internal current vector. A similar cost reduction can be noticed in the computation of the tangential stiffness matrix (cf. *Tangent Matrix*). Additionally, the computational time to solve the linear system (cf. *Linear Solve*) within the Newton-iteration scheme is significantly reduced.

Table 3. Computational times of different simulation steps for the three reduced-order models compared with the full training simulation.

	Full	**ECSW**		
		$\tau = 1 \times 10^{-2}$	$\tau = 1 \times 10^{-3}$	$\tau = 1 \times 10^{-4}$
No. of Elements	27,466	60	139	273
Element Selection Time	-	11 s	39 s	111 s
Residual	45 ms	6 ms	7 ms	7 ms
Tangent Matrix	95 ms	2 ms	3 ms	3 ms
Linear Solve	62 ms	0.1 ms	0.1 ms	0.1 ms
Total Simulation Time	150 s	38 s	39 s	40 s

It should be noted that some overhead during the solution process cannot be avoided. Thus, the real simulation of the reduced model does not completely scale with the number of elements. In summary, the required computational resources can be strongly decreased by the ECSW method while the allowed error on the internal energy during training is small.

4.5. Validation of the Model

To prove the ability of the reduced models, different load cases are now applied to the reduced models and the resulting force curve is compared against a full simulation with the same parameters. The quantitative measure for the comparison is a relative error (RE) for the force computed over all timesteps t_i along the test load case as follows:

$$RE = \frac{\sqrt{\sum_i (F_{ref}(t_i) - F(t_i))^T (F_{ref}(t_i) - F(t_i))}}{\sqrt{\sum_i F_{ref}(t_i)^T F_{ref}(t_i)}} \times 100\,\% \tag{25}$$

Throughout this paper, the time signal of the load is chosen as a sine. On the one hand, this is practicable for the test rig as well as for the simulation. On the other hand, it is very close to the load case expected for active magnetic bearings in applications.

The resulting reduced models achieved by the ECSW method offer some very interesting benefits in comparison to purely data-driven black box models. One point is that the same reduced system can also be used for different positions of the rotor in the bearing as the model still contains the geometric information. Furthermore, different timestep sizes do not influence the model. In addition, since the model is still physics-based (the data are only used to train the hyper-reduction of the forces, but the forces in the chosen element are still obtained from a model), one can expect that the reduced model will be able to extrapolate the behavior of the system better than purely data-driven models (e.g., a neural network).

In Table 4, exemplary results for the relative error of the mechanical force on the rotor are given for different parameters of a simple sine load case. The tested load cases are all different from the training cases. A first conclusion is drawn from the pure POD projection: the relative error is increasing with the frequency. The reason for it could in fact be that the mesh resolution is actually excessively coarse for higher frequencies. Second, the hyper-reduction does not introduce much new error to the model. In some cases, the error is even reduced which is explained by the fact that, by coincidence in our example, the errors due to the projection on a reduced space and the ones arising from the hyper-reduction are partly compensated for.

Table 4. Relative errors, always referred to in the full simulation reference, of the force for different parameters and excitations for each of the three hyper-reduction models.

	Full	**POD**	**ECSW**		
			$\tau = 1 \times 10^{-2}$	$\tau = 1 \times 10^{-3}$	$\tau = 1 \times 10^{-4}$
# dof	13,566	10	10	10	10
# els	27,466	27,466	60	139	273
		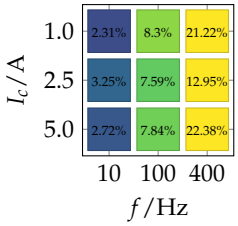	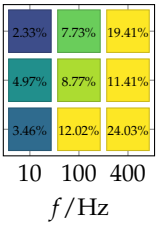	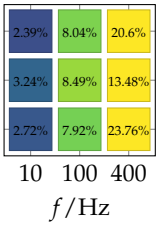	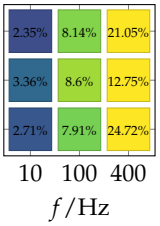

4.6. Intermediate Conclusions

The ECSW method has great potential since there are only a few elements which are necessary to accurately approximate the reduced forces. Further investigation needs to be conducted to find good training snapshots which span a wide field of parameters. Furthermore, the limitation of the mesh size needs to be improved. The optimization of the code would reveal higher time savings which scale better with the number of elements.

5. Experimental Validation

In the previous sections, a reduced-order model for the magnetic bearing was derived. In order to correctly predict the force exerted on the rotor, the parameters of the simulation model must be calibrated. For this purpose, a specialized test rig for the active magnetic bearing (AMB) is built.

5.1. Test Rig Overview

The test rig (Figure 9) carries the AMB mounted onto a 6-dof force measurement platform and a rotor that is not rotating and fixed in the center of the AMB. In the scope of this work, only the center position of the rotor is considered since it is the idle position in operation mode. Additionally to the force sensor, two current sensing clamps and temperature sensors are applied to measure the relevant quantities.

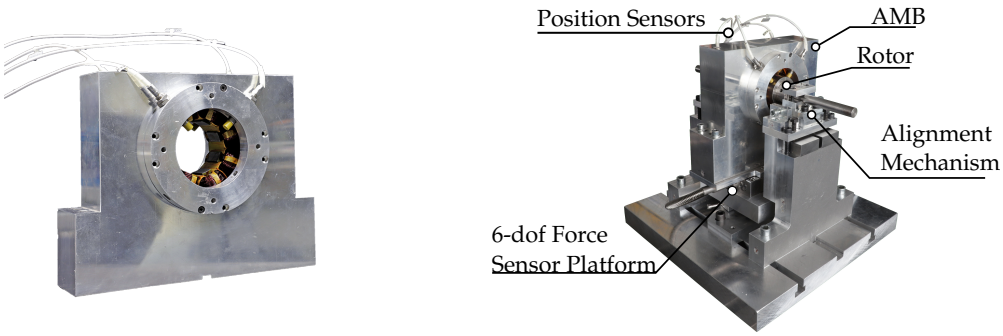

Figure 9. Active magnetic bearing and the experimental setup with a 6-dof force measurement platform and temperature sensors to calibrate the simulation in relation to measured forces and temperatures.

5.2. Model Calibration Strategy

Since multiple simplifications are used in the simulation model (2D simulation, no housing, isotropic materials), several parameters need to be calibrated using the real system. One approach could be to use any optimization algorithm to find a set of parameters optimal to an objective function. Unfortunately, this often leads to parameter sets that are not meaningful in a physical sense.

For this work, the identification of parameters is done stepwise, ordered such that each parameter is as isolated as possible. The investigated parameter is then fixed and the next is considered. With this procedure, the process of the dependent parameter determination is resolved to some extent, whereby only a suboptimal solution, but an interpretable one, can be found.

5.3. Static Model Parameters

5.3.1. Heat Coefficients

In the case of natural convection, values for a general heat transfer coefficient for an iron–air interface from $5\,\mathrm{W\,m^{-2}\,K^{-1}}$ to $25\,\mathrm{W\,m^{-2}\,K^{-1}}$ can be found in [14]. To perform an experimental calibration of the heat transfer coefficient of both the rotor and the stator, the magnetic bearing is heated up (using a sine trajectory with high current load) and the temperature decay is measured on the test rig. Multiple thermal simulations with varying

rotor and stator coefficients are performed to fit the simulation to the measurement. The chosen pair is given in Figure 10 where the solid line indicates the simulation and the diamond marks the measurements.

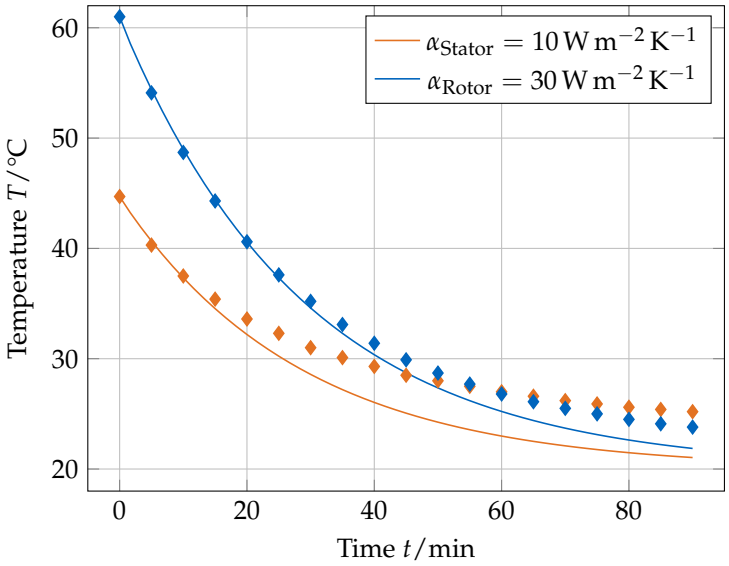

Figure 10. Calibration of heat transfer coefficients using the measured temperature decays.

5.3.2. Permeability

The core of the magnetic bearing consists of laminated non-oriented electrical steel sheets (M270-35A, 1.0801, $t = 0.35\,\text{mm}$). The nonlinear permeability $\mu(B)$ of the used material is assumed from datasheets (thyssenkrupp, M270-35A, DIN EN 10 106) approximated by continuous functions (as shown in Figure 3) and is fixed without further investigations for this work. The rotor is turned from low-carbon steel (S235JR, 1.0038).

5.3.3. Effective Thickness

To calculate meaningful force values from the 2D model, a thickness (=axial length) parameter is needed. The real geometric thickness is therefore modified using a factor ($t_{\text{eff}} = \kappa \cdot t_{\text{real}}$) that is determined using a static force simulation and corresponding measurements. The effective thickness also incorporates all effects of fringing and the fact that only approximately 95 % of the volume is filled with steel due to the stacking factor of the sheet lamination. κ is chosen such that static force simulations (no eddy currents occur) fit with the corresponding measurements. The measured force characteristic in Figure 11 was chosen to be $\kappa = 0.85$, resulting in a maximum force deviation of 7 N.

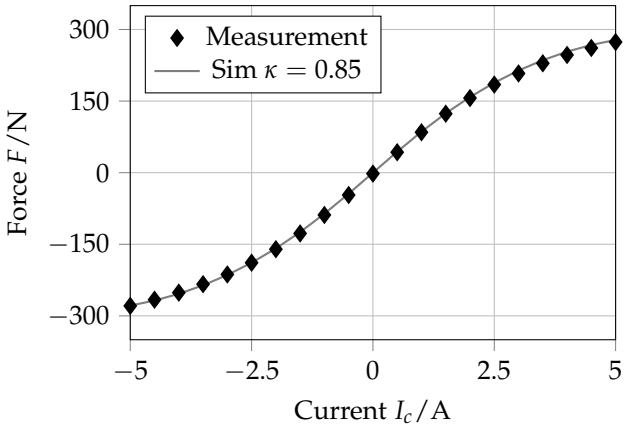

Figure 11. Resulting static magneto-static force obtained by simulation with an effective thickness of the bearing to compensate for leakage and fringing effects (comparison to measured forces).

5.4. Dynamic Model Parameters

Fixing the thus far parameterized static simulation, the electrical conductivity for the rotor and stator is calibrated in the dynamic regime. To do so, a long time integration simulation is set up with the shown time integration strategy. The scheme was conducted with two different large timesteps ($\Delta T_j = 100\,\mathrm{s}$ and $\Delta T_j = 300\,\mathrm{s}$) resulting in the same graphs of the temperatures.

5.4.1. Heat Capacitance

In the used test rig, the rotor is much longer than the axial length of the bearing core. Therefore, a virtual heat capacitance for the 2D simulation was assumed to be 10 times higher than the datasheet parameter.

5.4.2. Electrical Conductivity

The most difficult parameter to calibrate is the electrical conductivity in the stator of the AMB. The awaited eddy currents are in the out-of-plane direction of the 2D simulation. As eddy current losses should naturally be avoided, iron cores in alternating field conditions are laminated from sheets (here thickness 0.35 mm) and bonded with non-conductive glue. The conductivity of a single sheet is approximately $2\,\mathrm{MS\,m^{-1}}$ to $5\,\mathrm{MS\,m^{-1}}$. For the stack of sheets, a substitute model has to fulfill the requirement that the power loss as well as the magnetic field outside the core equals the correct model. Due to the skin effect (cf. Section 3.1), the relation between the sheet thickness and eddy current influence length will vary with frequency. This inevitably leads to a frequency-dependent parameter [15]. The penetration depth of Equation (15) indicates the length after which the electromagnetic field has decayed by a factor of $\frac{1}{e} \approx 37\,\%$. A short overview of the penetration depth for an exemplary set of parameters is given in Table 5.

Table 5. Eddy current penetration depth for $\mu = 5000$, $\sigma = 5\,\mathrm{MS\,m^{-1}}$.

f	$\delta(f)$
10 Hz	1 mm
100 Hz	0.3 mm
1 kHz	0.1 mm

Low frequencies lead to higher depths but in principle have less power in eddy currents. At high frequencies, the eddy currents are at the boundaries which in the extreme case would lead to full conductivity as the skin depth is smaller or equal to the sheet thickness. Introducing the lamination of cores into a nonlinear 2D simulation is still under research, and a solution is shown in [16].

For this work, a bulk lamination model is used which treats the material as a continuum and replaces the laminated core by a reduced constant conductivity in the direction normal to the sheets [15]. Our simulation and model order reduction framework have not supported frequency-dependent parameters to date. The extension to implement frequency-dependent conductivity would go beyond the scope of this work which focuses on the full round trip from the model to monitoring.

This parameterization needs very strong assumptions that are explainable in principle but can only be quantified using a calibration test rig. The focus was set upon choosing meaningful values by hand, so no optimization algorithm was involved. According to the formula given in [15], the conductivity is roughly reduced by a factor of 100 in contrast to the full material for the given geometry. Figure 12 shows the temperature development in the stator and rotor of the AMB for an excitation of 400 Hz and $I_c = 5\,\mathrm{A}$.

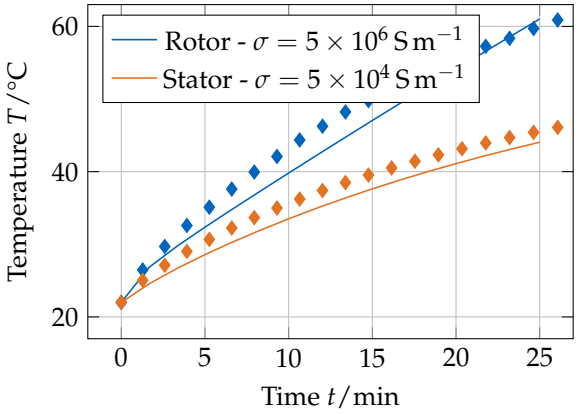

Figure 12. Temperature development in the magnetic bearing for an excitation of 400 Hz and $I_c = 5$ A.

5.5. Final Parameter Check

With that last parameter set, a final comparison of the measurement and simulation is performed by the investigation of an accidentally discovered effect. Whilst plotting one period (excitation $f = 400$ Hz) of the force on the rotor from time to time during a long-term experiment, an interesting effect of temperature-dependent force was observed (Figure 13) which could seem unintuitive at first glance. The force increases with the increasing temperatures of the stator and the rotor.

Using the above-parameterized simulation, the effect shall be proven to not be a test rig artifact. The peak-to-peak force is therefore plotted against the experiment time Figure 14. Note that the temperature for the rotor and stator evolve differently during long experiments (as seen in Figure 12). Due to the decreasing conductivity, less power loss is generated by the induced eddy currents. This leads to a higher force on the rotor.

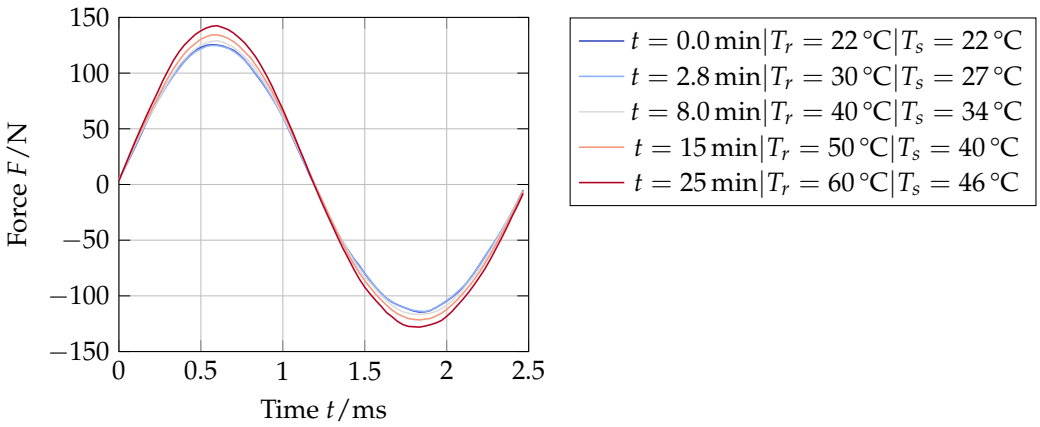

Figure 13. Measured force values at $f = 400$ Hz plotted over one period at different time points and temperatures.

The simulation yields the same qualitative behavior but the effect is significantly less pronounced. This may be for several reasons. The most obvious one is the attempt to represent a complex 3D environment using 2D simulation and appropriate factors. A second factor for this experiment is the mesh grid that is actually excessively coarse to be able to reliably represent frequencies up to 400 Hz and so the eddy currents in the skin will be underestimated. Furthermore, to draw useful information from the test, the temperatures were set to individually predefined values that spanned the typically maximum operation temperatures of active magnetic bearings that seem harmless. The results are also given in Figure 14.

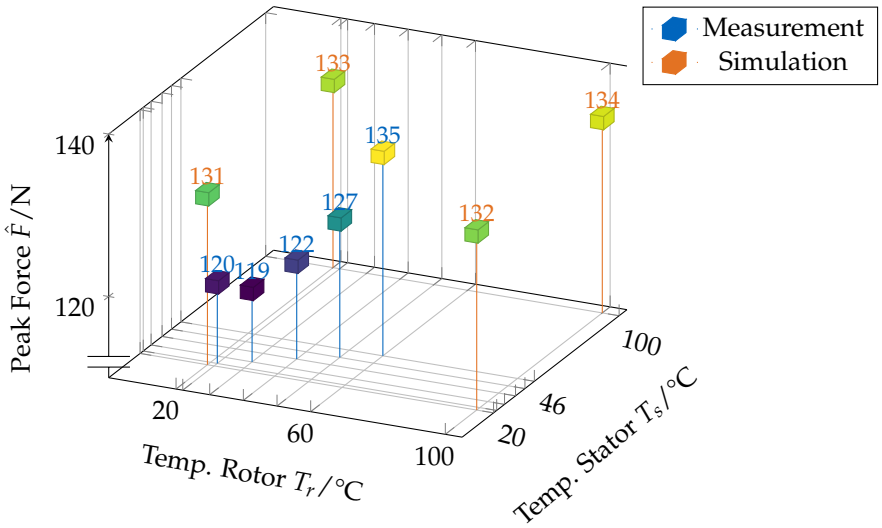

Figure 14. Increase of measured and simulated peak force values over different combinations of temperatures in rotor and stator. The simulation can show the qualitative effect compared to the measured values but less pronounced.

6. Summary and Conclusions

6.1. Summary

The presented work includes a full round trip of modeling, parameterization, model order reduction, and a proposed use of the model for monitoring an active magnetic bearing. Key to enabling long-duration coupled simulations was the use of two timestep sizes. The magnetodynamic simulation was conducted only every nth thermodynamic step. Additionally, the hyper-reduction brought massive savings for the magnetodynamic simulation. During the calibration with the experimental setup, the most severe limitation seemed to be the restriction to a 2D model. However, globally, all effects of the measured forces could be explained and rebuilt with the simulation. Although a well-trained black-box model could eventually have led to a similar result, the shown white box approach shown herein brings very detailed engineering insights and the modeling approach can be used to accurately model different geometries without needing a full new calibration.

6.2. Conclusions

The shown hyper-reduction method has the potential to drastically reduce magnetodynamic systems. To use such detailed models in future monitoring systems, good parameterization is essential. It was found that this was the most challenging point in this work. The experimental study showed basic agreement with the simulation. However, there is always the question of the trust level of the different parameters. This leads to the basic question of how detailed a full-order model has to be to represent all necessary physical effects for the desired purpose. In our opinion, more research is needed to find good and robust theoretical models to describe the relevant physical behavior of magnetodynamic systems in terms of smart monitoring systems. The successive step of model order reduction served well and is therefore useful after determining and parameterizing a full-order model.

Author Contributions: Conceptualization, J.M.; methodology, J.M.; software, J.M. and C.D.; validation, J.M.; formal analysis, C.D.; investigation, J.M., C.D. and O.M.Z.; resources, D.J.R.; data curation, J.M. and O.M.Z.; writing—original draft preparation, J.M. and C.D.; writing—review and editing, J.M., O.M.Z. and D.J.R.; visualization, J.M.; supervision, D.J.R. All authors have read and agreed to the published version of the manuscript.

Funding: This research received no external funding.

Institutional Review Board Statement: Not applicable.

Informed Consent Statement: Not applicable.

Data Availability Statement: Data available on request.

Conflicts of Interest: The authors declare no conflict of interest.

References

1. Faraji, F.; Majazi, A.; Al-Haddad, K. A comprehensive review of Flywheel Energy Storage System technology. *Renew. Sustain. Energy Rev.* **2017**, *67*, 477–490. [CrossRef]
2. Schweitzer, G.; Traxler, A.; Bleuler, H. *Magnetlager: Grundlagen, Eigenschaften und Anwendungen Berührungsfreier, Elektromagnetischer Lager*; Springer: Berlin/Heidelberg, Germany, 2013.
3. Shi, W.; Dustdar, S. The Promise of Edge Computing. *Computer* **2016**, *49*, 78–81. [CrossRef]
4. Varghese, B.; Wang, N.; Barbhuiya, S.; Kilpatrick, P.; Nikolopoulos, D.S. Challenges and Opportunities in Edge Computing. In Proceedings of the 2016 IEEE International Conference on Smart Cloud (SmartCloud), New York, NY, USA, 18–20 November 2016; IEEE: Piscataway, NJ, USA, 2016. [CrossRef]
5. Maierhofer, J.; Rixen, D.J. Model Order Reduction using Hyperreduction Methods (DEIM, ECSW) for Magnetodynamic FEM Problems. *Finite Elem. Anal. Des.* 2022, *in press*.
6. Vong, P.; Rodger, D. Coupled electromagnetic-thermal modeling of electrical machines. *IEEE Trans. Magn.* **2003**, *39*, 1614–1617. [CrossRef]
7. Jiang, Y.; Wang, D.; Zhang, Q.; Chen, J. Electromagnetic-Thermal Coupling Simulation by ANSYS Multiphysics of Induction Heater. *Appl. Mech. Mater.* **2014**, *701–702*, 820–825. [CrossRef]
8. Smallman, R.; Ngan, A. Physical Properties. In *Modern Physical Metallurgy*; Elsevier: Amsterdam, The Netherlands, 2014; pp. 317–356.[CrossRef]
9. Rudolph, M.; Schaefer, H. *Elektrothermische Verfahren: Grundlagen, Technologien, Anwendungen*; Springer: Berlin/Heidelberg, Germany, 1989.
10. Lide, D. *CRC Handbook of Chemistry and Physics*, 86th ed.; Taylor & Francis: Abingdon, UK, 2005.
11. Biro, O.; Preis, K. On the use of the magnetic vector potential in the finite-element analysis of three-dimensional eddy currents. *IEEE Trans. Magn.* **1989**, *25*, 3145–3159. [CrossRef]
12. Fetzer, J.; Haas, M.; Kurz, S. *Numerische Berechnung Elektromagnetischer Felder*, 1st ed.; Renningen: Malmsheim , Germany, 2002.
13. Farhat, C.; Avery, P.; Chapman, T.; Cortial, J. Dimensional reduction of nonlinear finite element dynamic models with finite rotations and energy-based mesh sampling and weighting for computational efficiency. *Int. J. Numer. Methods Eng.* **2014**, *98*, 625–662. [CrossRef]
14. Kosky, P.G.; Balmer, R.T.; Keat, W.; Wise, G. *Exploring Engineering an Introduction to Engineering and Design*; Academic Press: Cambridge, MA, USA, 2013; p. 462.
15. Hahne, P.; Dietz, R.; Rieth, B.; Weiland, T. Determination of anisotropic equivalent conductivity of laminated cores for numerical computation. *IEEE Trans. Magn.* **1996**, *32*, 1184–1187. [CrossRef]
16. Hollaus, K.; Hannukainen, A.; Schoberl, J. Two-Scale Homogenization of the Nonlinear Eddy Current Problem with FEM. *IEEE Trans. Magn.* **2014**, *50*, 413–416. [CrossRef]